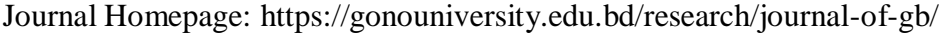
Journal of Gono Bishwabidyalay

ISSN: 2521-828X(Print) 2706-9303 (Online) 2706-9311(CD-ROM)





Original Research

Investigation of Structural and Morphological Properties of Hydrothermally Synthesized nanocomposites SnO₂/MoS₂

Md. Mostafa Kamal^{1*}, Md. Tushar Ahmed¹, Gazi Ishmam Hasan¹

Received: 04/01/2025; Accepted: 11/04/2025; Online Available: 18/08/2025.

Abstract

In this work, pure SnO₂ and SnO₂–MoS₂ nanocomposites were successfully synthesized via the hydrothermal method using a stainless-steel autoclave. The synthesis was carried out at a temperature of 140 °C and a pressure of 30 pounds per square inch (psi). The nanocomposites were characterized using X-ray diffraction (XRD), scanning electron microscopy (SEM), and Fourier transform infrared spectroscopy (FTIR). The formation of the nanocomposites was confirmed by both XRD patterns and SEM micrographs. The XRD results revealed that all samples exhibited a stable tetragonal SnO₂ phase. The crystallite size and lattice strain of the samples were investigated, with crystallite sizes ranging from 18.70 nm to 20.87 nm. A slight increase in crystallite size was observed with increasing MoS₂ content. The SEM micrographs confirmed the formation of non-uniform spherical particles. The average particle diameters for the 90% SnO₂–10% MoS₂, 80% SnO₂–20% MoS₂, and 70% SnO₂–30% MoS₂ samples were found to be 25.62 nm, 27 nm, and 31.21 nm, respectively. Similarly, the corresponding average particle areas were measured as 462.32 nm², 503.2 nm², and 548.32 nm², respectively. The FTIR spectra confirmed the formation of stable tetragonal SnO₂, and the vibrational behavior of the chemical bonds was also investigated.

Keywords— Tin (IV) oxide nanoparticles (SnO₂), Molybdenum disulfide nanoparticles (MoS₂), XRD, SEM, FTIR

Introduction

Tin dioxide (SnO2), an n-type wide-bandgap semiconductor with a bandgap of (3.6–4.0 eV), has acquired significance in nanotechnology owing to its exceptional optoelectronic characteristics, elevated carrier mobility, and chemical stability [1, 9]. Its versatility includes applications in gas sensing [5, 6], photocatalysis [10–14], energy storage [4, 15], and solar cells [9], enabled by its adjustable surface shape and defect-mediated functions [2, 17]. Recent studies highlight the efficacy of SnO2 in hybrid composites, where synergistic interactions improve charge separation and interfacial activity, essential for environmental remediation and energy conversion [4, 13]. SnO2-based heterostructures exhibit enhanced photocatalytic degradation of organic contaminants under visible light, underscoring their potential to tackle energy and environmental issues. Molybdenum disulfide (MoS₂), a layered transition metal dichalcogenide, improves SnO₂ due to its high surface-to-volume ratio, tunable bandgap (1.2–1.9 eV), and catalytic edge sites [16, 21]. The combination of MoS₂

¹ Department of Physics, Gono Bishwabidyalay, Savar, Dhaka 1344.

^{*} Corresponding Author: Md. Mostafa Kamal; Email: mostafaphysicsju@gmail.com; Mobile: +8801571424588.

and SnO₂ employs interfacial band alignment, enhancing electron-hole separation and photoresponse [14, 15]. Previous studies have demonstrated the production of composites through sol-gel and chemical vapor deposition (CVD) methods; however, these techniques often involve high energy costs, poor stoichiometric control, and limited scalability. Hydrothermal synthesis presents a practical alternative, enabling precise control over morphology, facilitating low-temperature processing, and promoting environmentally sustainable practices [19, 23]. Nonetheless, the regulated hydrothermal synthesis of SnO₂/MoS₂ nanocomposites with systematic compositional variation remains insufficiently explored, particularly regarding structural evolution and morphological interdependence [4, 13]. Recent research has revealed several significant deficiencies in the comprehension of SnO₂/MoS₂ systems: (i) the mechanisms regulating crystallite growth during hydrothermal treatment are insufficiently clarified [9,13]; (ii) enduring inconsistencies persist between crystallite sizes measured by XRD and particle sizes observed through SEM, frequently ascribed to agglomeration but seldom quantified [36, 41]; and (iii) the impacts of lattice strain and full-width at half maximum on charge transport have not been comprehensively examined [22, 35]. Resolving these difficulties is crucial for enhancing the design of composites for practical devices. Asaithambi et al. [4] and Zhang et al. [14] exhibited improved supercapacitor and photocatalytic performance in SnO₂/MoS₂ nevertheless, their approaches were deficient in the precise compositional gradients required to establish a conclusive correlation between structure and characteristics. This study addresses these gaps by utilizing controlled hydrothermal synthesis to produce SnO₂/MoS₂ nanocomposites with 10–30 M% MoS₂ content. This study seeks to achieve three objectives: (i) employ XRD, SEM, and FTIR to elucidate the structural and morphological evolution of nanocomposites; (ii) quantify discrepancies between crystallite (XRD) and particle (SEM) sizes and correlate them with agglomeration phenomena; and (iii) assess lattice parameter shifts and functional group interactions to identify strain-induced factors. We illustrate the efficacy of our hydrothermal method in generating homogeneous composites with tailored surfaces by comparing it to sol-gel and CVD approaches [8, 18]. This represents progress in the design of scalable nanomaterials for energy applications.

Experimental

The nanocomposites of SnO_2 -MoS₂ were synthesized by using an autoclave-assisted synthesis process, named hydrothermal synthesis. All the reagents were analytical grade, purchased from Sigma Aldrich, and used without further purification. The reagents involved in this process were stannic chloride pentahydrate [$SnCl_4.5H_2O$] as the precursor material and SnO_2 (AR grade, 99% pure, Sigma Aldrich Ltd., USA-made). Ammonium heptamolybdrate tetrahydrate (AR grade, > 98% pure, Sigma Aldrich Ltd., USA made) as a precursor of MoS_2 materials was added to the starting solution as a precursor for composite material. Thiourea [CH_4N_2S] as the precursor of the sulfur source (AR grade, > 98% pure, Sigma Aldrich Ltd., USA made). The other chemicals that were used for the preparation of samples, were concentrated sodium hydrogen carbonate ($NaHCO_3$) (AR grade, > 98% pure, Sigma Aldrich Ltd., USA made), vitamin C, and ethanol (C_2H_5OH).

SnO₂ nanoparticles preparation

Tin (IV) chloride pentahydrate [SnCl₄·5H₂O] was used as the precursor for synthesizing SnO₂ nanoparticles. A solution was prepared by dissolving 16.28 grams of SnCl₄·5H₂O and 2.91 grams of citric acid in 240 mL of deionized (DI) water. This solution was stirred using a magnetic stirrer at 60–75 rpm for 1 hour at room temperature to achieve homogeneity. Then, 15.62 grams of sodium hydrogen carbonate was added, followed by another 30 minutes of stirring. Afterward, 10 mL of deionized water containing 6.084 grams of dissolved vitamin C was added, and the solution was stirred for an additional 50 minutes. The resulting solution was transferred to a Teflon-lined stainless-steel autoclave, sealed, and heated at 140 °C under a pressure of 30 psi (equivalent to 2.04138 atm) for 20 hours. After hydrothermal treatment, the system was allowed to cool to room temperature. The SnO₂ precipitates formed were separated by filtration, washed five times with distilled water to remove residual ions, and then washed with ethanol to aid in water removal. Finally, the product was dried at 80 °C in an electric oven for 8 hours, yielding SnO₂ nanoparticles in powder form.

Chemical reaction:

$$SnCl_4 + 4NaHCO_3 \rightarrow SnO_2 + 4NaCl + 4CO_2 + 2H_2O.....(1)$$
 [15]

MoS₂ nanosheets preparation

Ammonium heptamolybdrate tetrahydrate [(NH₄)₆Mo₇O₂₄·4H₂O] (7.721 grams) and citric acid were dissolved in 240 mL of DI water to prepare the MoS₂ precursor solution. The solution was stirred using a magnetic stirrer at 60–75 rpm and heated at 90 °C for 1 hour to ensure homogeneity. Several drops of ammonia solution (NH₄OH) were added dropwise to adjust the pH to around 4. Then, 7.54 grams of thiourea was added, followed by 30 minutes of continuous stirring. The resulting solution was transferred to a Teflon-lined stainless-steel autoclave, sealed, and heated at 140 °C and 30 psi for 20 hours. After the hydrothermal treatment, the solution was cooled to room temperature, yielding black MoS₂ precipitates. These were separated by filtration, washed five times with distilled water, and rinsed with ethanol to assist in water removal. Finally, the product was dried at 80 °C in an electric oven for 8 hours, resulting in MoS₂ nanosheets.

SnO₂/MoS₂ nanocomposite formation

The formation of SnO₂–MoS₂ nanocomposites was achieved by adding MoS₂ nanoparticles on SnO₂. The nanocomposites were prepared by using xM% SnO₂ (x = 90, 80, 70) and (100-x) M% MoS₂ weight ratio. Where M% represents the weight in percentage. In this synthesis technique, the amount of MoS₂ nanoparticle was dispersed in deionized water as shown in Table-2.1, followed by ultrasonication for around 30 minutes at 50 Hz. The prepared nanostructure was settled by centrifugation at 7000 rpm for 15 min to ensure good dispersion of MoS₂ nanoparticles. Subsequently, 90M% SnO₂, 80M% SnO₂, and 70M% SnO₂ weight amounts of SnO₂ nanoparticles were repeated in a solution containing MoS₂ nanoparticles and stirring. The obtained solution was shifted into a Teflon-lined stainless-steel autoclave. The autoclave was compactly closed and heated at 140°C with a pressure of 30 psi, which is

equivalent to 2.04138 atm, for 20 hours, then allowed to cool to room temperature. After finishing the hydrothermal treatment, the obtained solution was black precipitates. The precipitates were separated by filtration and washed five times with distilled water for removal of ionic remains in the final products. The resulting products were further washed with ethanol to facilitate water evaporation and finally dried at 80° C in an electric oven for 8 hours, obtaining the SnO_2 -MoS₂ nanoparticles.

By varying the MoS₂ content, a series of composites with different SnO₂:MoS₂ weight ratios were obtained:

Nanocomposite 1 - 90M% SnO₂ / 10M% MoS₂ Nanocomposite 2 - 80M% SnO₂ / 20M% MoS₂ Nanocomposite 3 - 70M% SnO₂ / 30M% MoS₂

Table 2.1: Combination ratio of the SnO_2 and MoS_2 .

Ratio (M%)	$SnO_2(g)$	$MoS_2(g)$	Total (g)
90%:10%	6.3	0.7	7.0
80%:20%	5.6	1.4	7.0
70%:30%	4.9	2.1	7.0

Result and Discussions

In this work, pure SnO₂ and SnO₂–MoS₂ nanocomposites were synthesized via a hydrothermal method using a stainless-steel autoclave. The reaction temperature and pressure were maintained at 140 °C and 30 psi, respectively. The samples were kept in the autoclave for approximately 20 hours. After completing the hydrothermal cycle, the samples were dried in an electric oven, yielding pure SnO₂ and SnO₂–MoS₂ nanocomposite powders. These nano powders were characterized using several techniques. X-ray diffraction (XRD) was used for structural and phase identification, scanning electron microscopy (SEM) was employed to evaluate the surface morphology and particle shape, and Fourier-transform infrared spectroscopy (FTIR) was used to identify functional groups in the pure and composite materials.

Crystallographic structural properties

The structural properties of the synthesized SnO_2 and SnO_2 — MoS_2 nanocomposites were investigated using an X-ray powder diffractometer (X'Pert PRO, Philips PW3040). From the XRD data, the full width at half maximum (FWHM) and crystallite size (D) were determined. XRD patterns were used to confirm the crystallographic phases of the as-synthesized products. Figure 3.1 shows the XRD patterns of pure SnO_2 nanoparticles and SnO_2 — MoS_2 nanocomposites with varying MoS_2 weights (M%). All diffraction peaks observed for pure SnO_2 were indexed to the tetragonal phase (JCPDS card no. 41–1445) [20], with lattice constants a = b = 4.74 Å and c = 3.19 Å. Prominent peaks at (110), (101), (211), and (301) planes appeared at Bragg angles of 26.67° , 33.67° , 51.80° , and 64.60° , respectively.

Additionally, MoS₂ peaks at (002), (100), and (101) planes were observed [21]. Low-intensity diffraction peaks appeared at (200) in all pure and composite samples. No impurity peaks were detected, indicating successful formation of SnO₂–MoS₂ composites. The peak intensities decreased with increasing MoS₂ content, and enhanced intensity of the (110), (101), and (211) planes indicated highly anisotropic growth [13, 20, 22, 23].

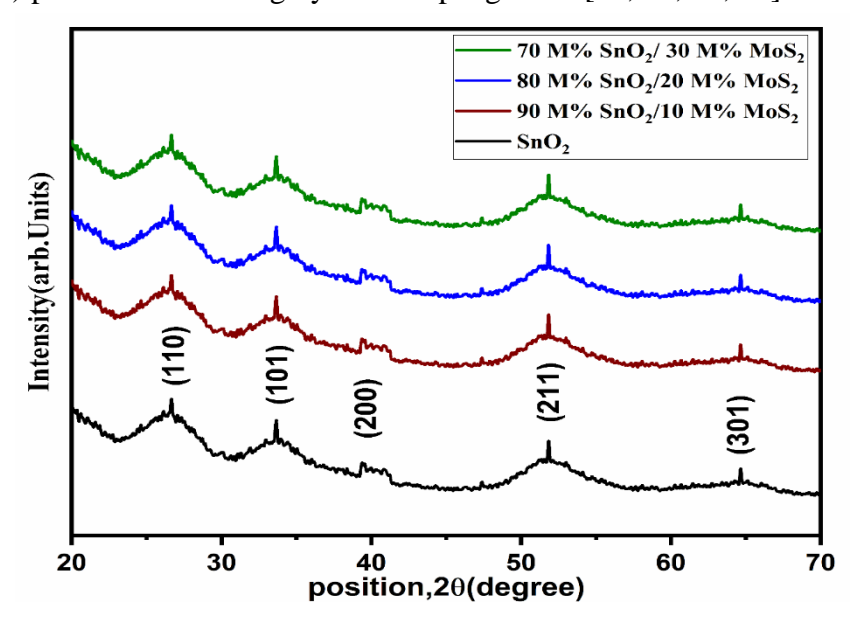


Figure 3.1 X-ray diffraction patterns of **(a)** pure SnO₂ (**black**) 90 M% SnO₂/10 M% MoS₂ (**red**), 80 M% SnO₂/20 M% MoS₂ (**blue**) and 70 M% SnO₂/30 M% MoS₂ (**green**) nanocomposites.

Lattice parameter

$$\frac{1}{d_{hkl}^2} = \frac{h^2}{a^2} + \frac{k^2}{b^2} + \frac{l^2}{c^2} \dots (3.1)$$

Where, d_{hkl} is the inter-planer spacing of the plane {h k l}. The inter-planar spacing of given Miller indices h, k and l. The inter-planer space d_{hkl} values were calculated by using the Bragg's equation [26]

$$2d_{hkl}\sin\theta_{hkl} = n\lambda....(3.2)$$

Where 'n' is the order of diffraction (usually n=1) and ' λ ' is the X-ray wavelength of Cu K_{\alpha1} radiation (λ =1.5406 Å) and ' Θ_{hkl} ' is the Brags diffraction angle.

Table 3.1: Diffraction angle, $2\theta_{hkl}$ (degree) of pure SnO₂ and SnO₂-MoS₂ nanocomposites.

Samples	Brags diffraction angle 2 0 hkl (deg)				
	2 0 ₁₁₀	2 0 101	2 0 ₂₁₁	2 0 ₃₀₁	
SnO ₂	26.67	33.67	51.8	64.6	
90M% SnO ₂ -10M% MoS ₂	26.64	33.63	51.78	64.57	
80M% SnO ₂ -20M%MoS ₂	26.69	33.68	51.84	64.62	
70 M%SnO ₂ -30M%MoS ₂	26.63	33.69	51.79	64.59	

In Table 3.1 and Table 3.2, the calculated diffraction angles and interplanner distances were tabulated. The hkl and d_{hkl} values for the Pure and deposited at different percentage concentrations are well matched with the values found in the JCPDS card. The calculated values of lattice parameters of pure SnO₂ lattice constants were a = b = 4.74 Å and c = 3.19 Å for tetragonal phase which are in good agreement with standard results and previous reported values [11, 27, 28, 29, 30].

Table 3.2: Inter planar distance d_{hkl} (nm) of pure SnO₂ and SnO₂-MoS₂ nanocomposites.

Samples	Inter planner distance, d _{hkl (nm)}				
	d_{110}	d_{101}	d ₂₁₁	d ₃₀₁	
SnO ₂	0.33397	0.26597	0.176337	0.14416	
90M%SnO ₂ -10M%MoS ₂	0.33652	0.26374	0.17267	0.14753	
80M%SnO ₂ -20M%MoS ₂	0.33537	0.26745	0.17569	0.14376	
70M%SnO ₂ -30M%MoS ₂	0.33643	0.26478	0.17634	0.14673	

Table 3.3: Lattice parameters and volume of unit cell of pure SnO₂ and SnO₂-MoS₂ nanocomposites obtained from XRD spectra.

Samples	Lattice parameter			b/a	b/c	c/a	Volume V(ų)	Ref.
	a (Å)	b(Å)	c(Å)					
SnO_2	4.7456	4.7456	3.1930	1	1.4862	0.6728	71.9086	[31]
90M%SnO ₂ -10M%MoS ₂	4.7354	4.7354	3.1892	1	1.4848	0.6734	71.5146	[32]
80M%SnO ₂ -20M%MoS ₂	4.7543	4.7543	3.1934	1	1.4887	0.6716	72.1816	[33]
70M%SnO ₂ -30M%MoS ₂	4.7646	4.7646	3.1827	1	1.4970	0.6679	72.2518	[33]

According to Tables 3.1 and 3.2, the diffraction angle and interplanar spacing distance somewhat as the MoS_2 content in the SnO_2 matrix vary. The lattice parameters are observed to be dependent on the SnO_2 percent concentration of MoS_2 . In Table 3.3 SnO_2 and SnO_2 - MoS_2 nanocomposites, the unit cell volume gradually increases as the percent concentration

of MoS_2 increases. SnO_2 - MoS_2 has the lowest unit cell volume of 71.9086 (Å)³ and the most significant unit cell volume of 72.2518 (Å)³ of 70M% SnO_2 -30M% MoS_2 percent.

Full-width at half maximum (FWHM)

The width of a line form at half of its highest amplitude is called the full width at half maximum (FWHM). The half-width at half maximum (HWHM), also known as the Resolving Resolution, is a closely related metric that is half of the FWHM. FWHM is the full-width at half maximum and θ is the Bragg angle. FWHM was calculated from the peak having the highest intensity in all the samples [34]. The FWHM is used to define resolution, and while the concept is simple, it is a critical quantity. If the FWHMs of two peaks overlap, they are unresolvable and appear to be one peak. In other words, it is the width of a spectrum curve measured between those points on the y-axis that are half of the maximum amplitude. FWHM is applied to such phenomena as the duration of pulse waveforms and particular width of sources used for optical communications and the resolution of spectrometers. The FWHM is a very an essential parameter that helps to analyze the X-ray diffraction patterns.

Table 3.4: Different FWHM, β_{hkl} (deg.) values pure SnO_2 and SnO_2 -MoS $_2$ nanocomposites.

Samples	Fullwidth at half maximum, β _{hkl} (degree)					
	$oldsymbol{eta}_{110}$	β_{101}	β_{211}	$m{eta}_{301}$		
SnO ₂	0.39604	0.38629	0.473045	0.666372		
90M%SnO ₂ -10M%MoS ₂	0.38527	0.36278	0.46245	0.66534		
80M%SnO ₂ -20M%MoS ₂	0.37854	0.35535	0.45834	0.66067		
70M%SnO ₂ -30M%MoS ₂	0.37253	0.35094	0.45123	0.65545		

The values of FWHM measured in degree of pure SnO_2 and SnO_2 -MoS₂ nanocomposites are listed in Table 3.4. These values of FWHM are used to calculate the crystallite size. The FWHM value can be found to fit with the Lorentzian function by origin software. With rising MoS_2 concentration, the whole breadth at half maximum value steadily decreases. As a result, the XRD peaks of pure SnO_2 and SnO_2 -MoS₂ nanocomposites from a higher to a lower angle as the MoS_2 concentration increases.

Crystallite size (D)

The mean size of single-crystal nanoparticles or crystallites in nanocrystalline bulk materials can be determined using X-ray diffraction. Paul Scherrer was the first to examine the influence of particle size limitations on X-ray diffraction patterns, and his findings were reported in a publication that included the Scherrer equation. This equation, however, appears to be incorrectly referred to as the 'Debye–Scherrer equation [35].

$$D = \frac{k\lambda}{\beta_{hkl}\cos\theta_{hkl}}$$
....(3.3)

Where, D, λ , k, β_{hkl} , θ_{hkl} are the crystallite size, the wavelength of X-ray radiation ($\lambda = 1.5406 \text{ Å}$ for Cu-k α), the shape factor and constant (k = 0.90), the full width half maximum (FWHM) of the brag's diffraction peak (in radians) located at 2 θ and the Bragg angle (in

degrees), respectively. In table 5.6, the various crystallite size values are described using Debye-Scherrer's approach. Size broadening is independent of the order of a reflection, as shown by equation (3.3). As the concentration of MoS_2 rises, so does the average crystallite size is increased [9, 36]. This result is in line with past investigations on pure SnO₂ and SnO₂-MoS₂ nanocomposites [9].

G 1	Cry	Average			
Samples	D_{110}	D_{101}	D ₂₁₁	D ₃₀₁	Crytallites size
					D _{hkl} ,(nm)
SnO_2	20.62	21.49	18.67	14.04	18.70
90M%SnO ₂ -10M%MoS ₂	21.19	22.87	19.09	14.12	19.31
80M%SnO ₂ -20M%MoS ₂	21.56	23.36	19.27	15.22	19.85
70M%SnO ₂ -30M%MoS ₂	22.92	23.65	20.57	16.35	20.87

Table 3.5: Crystallites size of pure and SnO₂- MoS₂ nanocomposites.

Surface Morphological Characteristics

Morphology

Scanning electron microscopy (SEM) is one of the most extensively utilized methods for analyzing nanomaterials and nanostructures. The signals generated by electron-sample interactions provide information about the sample, such as the sample's surface shape. grain size of nanocrystals mainly depends upon the relative rates of nucleation and growth processes, as well as the extent of agglomeration. The pH of the reaction mixture largely affects the size, shape, and morphology of the SnO₂ nanoparticles [37]. In this work, SnO₂ nanoparticle is synthesized by hydrothermal methods by adjusting PH around 7.5 by adding several drops of ammonia solution (NH₄OH). Prepared SnO₂, MoS₂ and SnO₂-MoS₂ nanocomposites are investigated by SEM model: JSM 7600F JEOL.

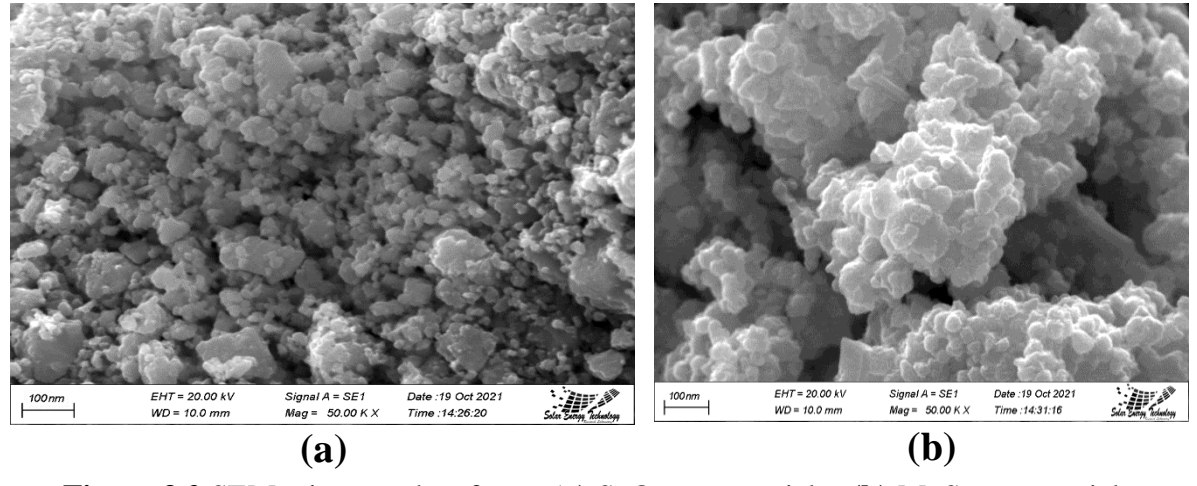


Figure 3.2 SEM micrographs of pure (a) SnO₂ nanoparticles (b) MoS₂ nanoparticles

It reveals randomly arranged irregular spherical sized [38, 39] compact grains with sponge like structure. Some deep pits are observed in morphology. Clustering of particles seems to

have occurred on the surface. In this image, cubic structures can be easily seen. It is now well established that different particle morphologies of nano-SnO₂, e.g., nanotube, nanobelt, and nanorod, uniform spherical and non- uniform spherical shape can be obtained under different synthesis conditions. The catalysts are formed of aggregate particles with a varied size distribution ranging between 22 and 31 nm nanoparticles, as shown by SEM micrographs of SnO₂ and SnO₂-MoS₂ nanoparticles. The agglomeration effect has an impact on the size of the particles. Agglomeration Occurs in Nanocomposites due to High Surface Energy, Van der Waals Forces and Solvent Effects or Drying During Sample Preparation [43].

Pure SnO₂ nanoparticles

Figure 3.2(a) shows the morphology of pure SnO₂ nanoparticles. The irregular spherical shaped SnO₂ nano particles with approximately non uniform size are shown in this SEM micrographs. The size was measured by **ImageJ software.** The average diameter and area of SnO₂ are 22.34nm and 433.93 nm², respectively the particles were agglomerated, as seen in the SEM image. This result is in line with past investigations on pure SnO₂ nanoparticles [40, 41].

Pure MoS₂ nanoparticles

Figure 3.2(b) shows the SEM micrograph of pure MoS_2 of nanoparticles synthesized using hydrothermal method. Many nanoparticles, especially the larger ones, exhibit a non-uniform growth shaped morphology. These non-uniform nanoparticles are aggregated each other. The average diameter and area of MoS_2 are 37.32nm and 582.5 nm².

SnO₂/MoS₂ composites

Figure 3.3 (a-c) shows the SEM micrographs of 90 M%SnO₂-10 M% MoS₂, 80 M%SnO₂-20 M%MoS₂ and 70 M%SnO₂-30 M%MoS₂ respectively. There are many nanoparticles. They are aggregated each another. Among them some nanoparticles are larger and clear shaped.

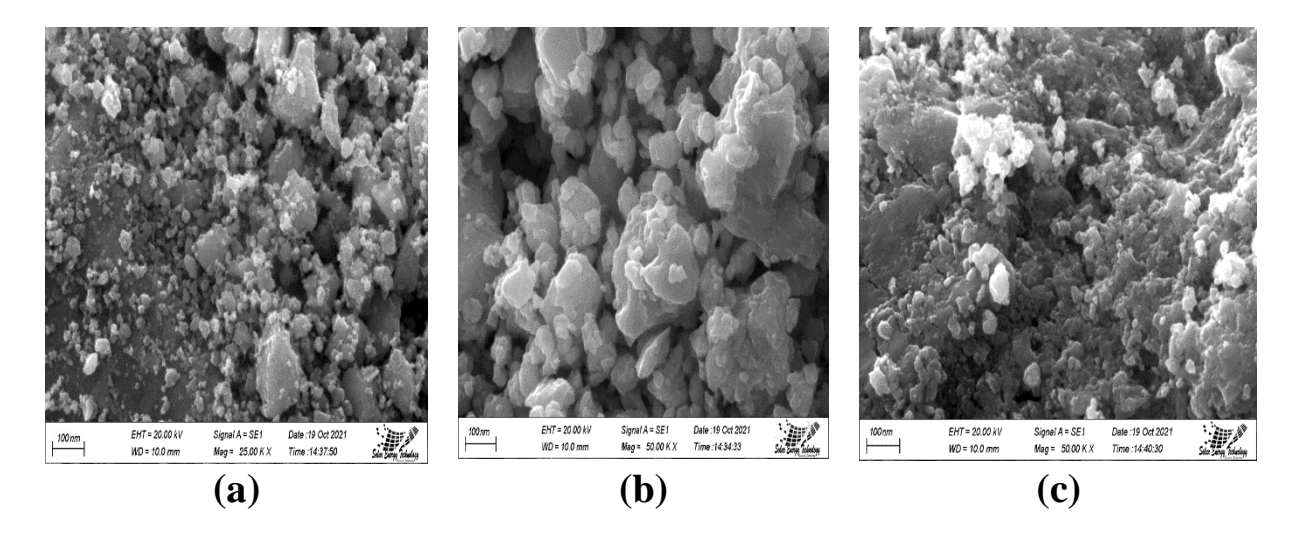


Figure 3.3 SEM micrographs of (a) 90 M%SnO₂-10 M% MoS₂ (b) 80 M%SnO₂-20 M%MoS₂ and (c) 70 M%SnO₂-30 M%MoS₂.

The average diameter are 25.62 nm, 27 nm and 31.21 nm respectively. The average area of the samples is 462.32 nm², 503.2 nm² and 548.32 nm² respectively. The average diameter and area of the SnO_2 -MoS₂ nanocomposites are gradually increased with the increasing of MoS₂ M%.

Functional group analysis

FTIR analysis is used to identify organic, inorganic, and polymeric materials utilizing infrared light for scanning the samples. Alterations in the characteristic pattern of absorption bands indicate a change in the material composition. FTIR helps identify and characterize

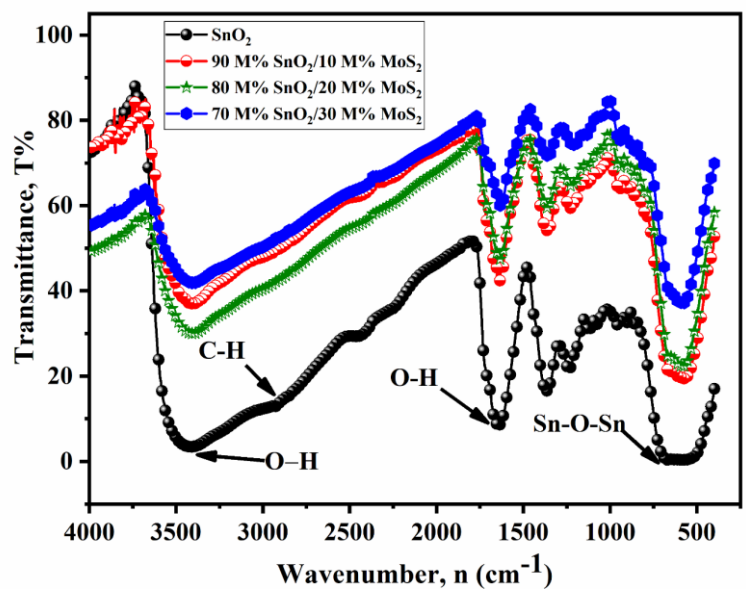


Figure 3.3: FTIR transmittance spectra of SnO₂, 90M%SnO₂-10M%MoS₂, 80M%SnO₂-20M%MoS₂ and 70M%SnO₂-30M%MoS₂.

unknown materials, detect contaminants in a material, find additives, and identify decomposition and oxidation. FTIR can collect high spectral resolution data over a wide range, usually between 4000 cm⁻¹ and 400 cm⁻¹ for mid-IR region wavelength and between 10,000 cm⁻¹ and 4000 cm⁻¹ for near-IR region wavelength. Fig. 3.3 shows the FTIR spectra of pure SnO₂ and SnO₂-MoS₂ nanocomposites. The strong O-H stretching vibration peak is observed at around 3428 cm⁻¹, and O-H bending vibration is appeared at 1646cm⁻¹. The weak absorption peak is observed at 2935 cm⁻¹ is related to the mode of C-H stretching vibration. The antisymmetric Sn-O-Sn mode and terminal Sn-O mode of vibration peak is attributed at 648 cm⁻¹ and 550 cm⁻¹, respectively. In the case of SnO₂-MoS₂ structures, only SnO₂ related absorption peaks are observed. There is no characteristic peak of MoS₂, which may be due to the small MoS₂ incorporated into these composites. This result is in line with past investigations on pure SnO₂ and SnO₂- MoS₂ nanocomposites as reported in the published articles [4, 9, 42].

Conclusion and Future Directions

In this study, pure SnO₂ and SnO₂–MoS₂ nanocomposites were successfully synthesized using a hydrothermal method. Characterization was conducted using XRD, SEM, and FTIR

techniques. XRD analysis confirmed the tetragonal phase of SnO₂ and allowed determination of lattice strain and crystallite size using the Williamson–Hall and Scherrer methods, respectively. Crystallite sizes increased from 18.70 nm to 20.87 nm with higher MoS₂ content. SEM images revealed irregular spherical morphologies and increasing particle size with MoS₂ incorporation. The difference between crystallite and particle sizes may be attributed to agglomeration. FTIR spectra identified O–H, C–H, and Sn–O–Sn vibrational modes. The future prospects of this research include the determination of the optical bandgap of SnO₂–MoS₂ nanocomposites using UV-vis spectroscopy. Additionally, the electrical conductivity of the nanocomposites can be measured by preparing thin films and employing the four-point probe method. These investigations may further support the potential application of the material in solar cell technology.

Authors Contributions

Conceptualization, study design and writing-original draft were contributed by Md. Mostafa Kamal. Data entry, Table and figure preparation were done by Md. Tushar Ahmed and Gazi Ishmam Hasan. All authors have read and agreed to the published version of the manuscript.

Acknowledgements

The authors would like to express their sincere gratitude to the Atomic Energy Research Establishment (AERE), Savar, Dhaka-1349 and Department of Physics, Gono Bishwabidyalay Savar, Dhaka-1344 for their constant support to complete this article.

Conflict of interest

The authors declare that they do not have any conflict of interest.

References

- 1. O. Lupan, L. Chow, G. Chai, H. Heinrich, S. Park, A. Schulte, Synthesis of one-dimensional SnO₂ nanorods via a hydrothermal technique, Physica E: Low-dimensional Systems and Nanostructures, Volume 41, Issue 4, 2009, Pages 533-536, ISSN 1386-9477, https://doi.org/10.1016/j.physe.2008.10.001.
- M. Mostafa and E. A. Mwafy, "Effect of dual-beam laser radiation for synthetic SnO₂/Au nanoalloy for antibacterial activity," *J. Mol. Struct.*, vol. 1222, p. 128913, 2020, doi: 10.1016/j.molstruc.2020.128913.
- 3. S. J. Hazarika and D. Mohanta, "Inorganic fullerene-type WS₂ nanoparticles: processing, characterization and its photocatalytic performance on malachite green," *Appl. Phys. Mater. Sci. Process.*, vol. 123, no. 5, 2017, doi: 10.1007/s00339-017-0965-7.
- 4. S. Asaithambi *et al.*, "Synthesis and characterization of various transition metals doped SnO₂@MoS₂ composites for supercapacitor and photocatalytic applications," *J. Alloys Compd.*, vol. 853, p. 157060, 2021, doi: 10.1016/j.jallcom.2020.157060.
- 5. M. Nanocomposite, A. T. L. Range, M. N. Electronics, and S. Jiao, "AN ULTRASENSITIVE HUMIDITY SENSOR BASED ON SnO₂ -MODIFIED," vol. 2, no. January, pp. 912–915, 2018.
- 6. H. Yan, P. Song, S. Zhang, Z. Yang, and Q. Wang, "Dispersed SnO₂ nanoparticles on MoS₂ nanosheets for superior gas-sensing performances to ethanol," *RSC Adv.*, vol. 5, no. 97, pp. 79593–79599, 2015, doi: 10.1039/c5ra15019a.
- 7. S. Bai, D. Li, D. Han, R. Luo, A. Chen, and C. L. Chung, "Preparation, characterization of WO₃-SnO₂ nanocomposites and their sensing properties for NO₂," *Sens. Actuators B Chem.*, vol. 150, no. 2, pp. 749–755, 2010, doi: 10.1016/j.snb.2010.08.007.

- 8. J. Huang, X. Wang, S. Li, and Y. Wang, "ZnO/MoO₃ mixed oxide nanotube: A highly efficient and stable catalyst for degradation of dye by air under room conditions," *Appl. Surf. Sci.*, vol. 257, no. 1, pp. 116–121, 2010, doi: 10.1016/j.apsusc.2010.06.046.
- 9. P. Chetri and A. Choudhury, "Investigation of optical properties of SnO₂ nanoparticles," *Phys. E Low-Dimens. Syst. Nanostructures*, vol. 47, pp. 257–263, 2013, doi: 10.1016/j.physe.2012.11.011.
- 10. [10]. A. Rani *et al.*, "Visible light driven photocatalysis of organic dyes using SnO₂ decorated MoS₂ nanocomposites," *Chem. Phys. Lett.*, vol. 738, p. 136874, 2020, doi: 10.1016/j.cplett.2019.136874.
- 11. S. P. Kim, M. Y. Choi, and H. C. Choi, "Photocatalytic activity of SnO₂ nanoparticles in methylene blue degradation," *Mater. Res. Bull.*, vol. 74, pp. 85–89, 2016, doi: 10.1016/j.materresbull.2015.10.024.
- 12. M. Ben Ali *et al.*, "Preparation and characterization of Ni-doped ZnO-SnO₂ nanocomposites: Application in photocatalysis," *Superlattices Microstruct.*, vol. 91, pp. 225–237, 2016, doi: 10.1016/j.spmi.2016.01.014.
- 13. X. Ni, C. Chen, Q. Wang, and Z. Li, "One-step hydrothermal synthesis of SnO₂-MoS₂ composite heterostructure for improved visible light photocatalytic performance," *Chem. Phys.*, vol. 525, no. May, p. 110398, 2019, doi: 10.1016/j.chemphys.2019.110398.
- 14. X. Zhang, Y. Yang, S. Ding, W. Que, Z. Zheng, and Y. Du, "Construction of High-Quality SnO₂@MoS₂ Nanohybrids for Promising Photoelectrocatalytic Applications," *Inorg. Chem.*, vol. 56, no. 6, pp. 3386–3393, 2017, doi: 10.1021/acs.inorgchem.6b02914.
- 15. L. Ma, X. Zhou, L. Xu, X. Xu, and L. Zhang, "Microwave-Assisted Hydrothermal Preparation of SnO₂/MoS₂ Composites and their Electrochemical Performance," *Nano*, vol. 11, no. 2, pp. 16–18, 2016, doi: 10.1142/S1793292016500235.
- 16. Muhammad Yousaf, Asif Mahmood, Yunsong Wang, Yijun Chen, Zhimin Ma, and Ray P. S. Han, "Advancement in Layered Transition Metal Dichalcogenide Composites for Lithium and Sodium Ion Batteries," *J Electr. Eng.*, vol. 4, no. 2, pp. 58–74, 2016, doi: 10.17265/2328-2223/2016.02.003.
- 17. W. Z. Xiao, G. Xiao, and L. L. Wang, "A first-principles study of the SnO₂ monolayer with hexagonal structure," *J. Chem. Phys.*, vol. 145, no. 17, 2016, doi: 10.1063/1.4966581.
- 18. A. Patel, B. Roondhe, and P. K. Jha, "Ni doping effect on the electronic and sensing properties of 2D SnO₂," *AIP Conf. Proc.*, vol. 1961, pp. 1–7, 2018, doi: 10.1063/1.5035241.
- 19. A. Mamakhel, M. Søndergaard, K. Borup, and B. Brummerstedt Iversen, "Continuous flow hydrothermal synthesis of rutile SnO₂ nanoparticles: Exploration of pH and temperature effects," *J. Supercrit. Fluids*, vol. 166, pp. 1–8, 2020, doi: 10.1016/j.supflu.2020.105029.
- 20. T. M. Al-saadi, "Preparation and Study Effects of Stirring Time on the Structural and Optical Properties of SnO₂ Nanoparticles," *Eng TechJournal*, vol. 33, no. 5, pp. 960–972, 2015.
- 21. P. K. Panigrahi and A. Pathak, "Aqueous Medium Synthesis Route for Randomly Stacked Molybdenum Disulfide," *J. Nanoparticles*, vol. 2013, pp. 1–10, 2013, doi: 10.1155/2013/671214.
- 22. F. A. Akgul *et al.*, "Structural and electronic properties of SnO₂," *J. Alloys Compd.*, vol. 579, pp. 50–56, 2013, doi: 10.1016/j.jallcom.2013.05.057.
- 23. N. Talebian and F. Jafarinezhad, "Morphology-controlled synthesis of SnO₂ nanostructures using hydrothermal method and their photocatalytic applications," *Ceram. Int.*, vol. 39, no. 7, pp. 8311–8317, 2013, doi: 10.1016/j.ceramint.2013.03.101.
- 24. M. Varshney, A. Sharma, R. Kumar, and K. D. Verma, "Swift heavy ion irradiation induced nanoparticle formation in CeO₂ thin films," *Nucl. Instrum. Methods Phys. Res. Sect. B Beam Interact. Mater. At.*, vol. 269, no. 23, pp. 2786–2791, 2011, doi: 10.1016/j.nimb.2011.09.001.
- 25. S. Tazikeh, A. Akbari, A. Talebi, and E. Talebi, "Synthesis and characterization of tin oxide nanoparticles via the Co-precipitation method," *Mater. Sci.- Pol.*, vol. 32, no. 1, pp. 98–101, 2014, doi: 10.2478/s13536-013-0164-y.
- 26. J. Epp, X-Ray Diffraction (XRD) Techniques for Materials Characterization. Elsevier Ltd, 2016. doi: 10.1016/B978-0-08-100040-3.00004-3.
- 27. G. Z. Xing *et al.*, "Hybrid CuO/SnO₂ nanocomposites: Towards cost-effective and high performance binder free lithium ion batteries anode materials," *Appl. Phys. Lett.*, vol. 105, no. 14, 2014, doi: 10.1063/1.4896256.
- 28. M. S. Morassaei, S. Zinatloo-Ajabshir, and M. Salavati-Niasari, "New facile synthesis, structural and photocatalytic studies of NdOCl-Nd₂Sn₂O₇-SnO₂ nanocomposites," *J. Mol. Liq.*, vol. 220, pp. 902–909, 2016, doi: 10.1016/j.molliq.2016.05.041.
- 29. R. K. Mishra and P. P. Sahay, "Synthesis, characterization and alcohol sensing property of Zn-doped SnO₂ nanoparticles," *Ceram. Int.*, vol. 38, no. 3, pp. 2295–2304, 2012, doi: 10.1016/j.ceramint.2011.10.081.

- 30. A. Hamrouni, H. Lachheb, and A. Houas, "Synthesis, characterization and photocatalytic activity of ZnO-SnO₂ nanocomposites," *Mater. Sci. Eng. B Solid-State Mater. Adv. Technol.*, vol. 178, no. 20, pp. 1371–1379, 2013, doi: 10.1016/j.mseb.2013.08.008.
- 31. S. S. Chang, S. O. Yoon, and H. J. Park, "Characteristics of SnO₂ annealed in reducing atmosphere," *Ceram. Int.*, vol. 31, no. 3, pp. 405–410, 2005, doi: 10.1016/j.ceramint.2004.05.026.
- 32. T. M. Al-Saadi, B. H. Hussein, A. B. Hasan, and A. A. Shehab, "Study the structural and optical properties of Cr doped SnO₂ nanoparticles synthesized by sol-gel method," *Energy Procedia*, vol. 157, no. 2018, pp. 457–465, 2019, doi: 10.1016/j.egypro.2018.11.210.
- 33. M. Karmaoui *et al.*, "One-Step Synthesis, Structure, and Band Gap Properties of SnO₂ Nanoparticles Made by a Low Temperature Nonaqueous Sol-Gel Technique," *ACS Omega*, vol. 3, no. 10, pp. 13227–13238, 2018, doi: 10.1021/acsomega.8b02122.
- 34. E. Abdelkader, L. Nadjia, B. Naceur, and B. Noureddine, "SnO₂ foam grain-shaped nanoparticles: Synthesis, characterization and UVA light induced photocatalysis," *J. Alloys Compd.*, vol. 679, pp. 408–419, 2016, doi: 10.1016/j.jallcom.2016.04.016.
- 35. X. Zhong, B. Yang, X. Zhang, J. Jia, and G. Yi, "Effect of calcining temperature and time on the characteristics of Sb-doped SnO₂ nanoparticles synthesized by the sol-gel method," *Particuology*, vol. 10, no. 3, pp. 365–370, 2012, doi: 10.1016/j.partic.2011.09.005.
- 36. V. Kumar *et al.*, "Effect of solvent on crystallographic, morphological and optical properties of SnO₂ nanoparticles," *Mater. Res. Bull.*, vol. 85, pp. 202–208, 2017, doi: 10.1016/j.materresbull.2016.09.020.
- 37. A. G. Habte, F. G. Hone, and F. B. Dejene, "Effect of solution pH on structural, optical and morphological properties of SnO₂ nanoparticles," *Phys. B Condens. Matter*, vol. 580, 2020, doi: 10.1016/j.physb.2019.411832.
- 38. J. Mayandi, M. Marikkannan, V. Ragavendran, and P. Jayabal, "Hydrothermally Synthesized Sb and Zn Doped SnO₂ Nanoparticles," vol. 2, no. 6, pp. 707–710, 2014.
- 39. S. M. Hassan, A. I. Ahmed, and M. A. Mannaa, "Structural, photocatalytic, biological and catalytic properties of SnO₂/TiO₂ nanoparticles," *Ceram. Int.*, vol. 44, no. 6, pp. 6201–6211, 2018, doi: 10.1016/j.ceramint.2018.01.005.
- 40. M. S. Park, Y. M. Kang, G. X. Wang, S. X. Dou, and H. K. Liu, "The effect of morphological modification on the electrochemical properties of SnO₂ nanomaterials," *Adv. Funct. Mater.*, vol. 18, no. 3, pp. 455–461, 2008, doi: 10.1002/adfm.200700407.
- 41. P. Khaenamkaew, D. Manop, C. Tanghengjaroen, and W. Palakawong Na Ayuthaya, "Crystal Structure, Lattice Strain, Morphology, and Electrical Properties of SnO₂ Nanoparticles Induced by Low Calcination Temperature," *Adv. Mater. Sci. Eng.*, vol. 2020, 2020, doi: 10.1155/2020/3852421.
- 42. A. Azam, A. S. Ahmed, S. S. Habib, and A. H. Naqvi, "Effect of Mn doping on the structural and optical properties of SnO₂ nanoparticles," *J. Alloys Compd.*, vol. 523, pp. 83–87, 2012, doi: 10.1016/j.jallcom.2012.01.072.
- 43. Ong, C., Lee, W.N., Tan, Y.S. et al. Optical bandgap tuning in SnO₂–MoS₂ nanocomposites: manipulating the mass of SnO₂ and MoS₂ using sonochemical solution mixing. J Mater Sci: Mater Electron 36, 6 (2025). https://doi.org/10.1007/s10854-024-14061-7